

pubs.acs.org/JACS Article

Chemical Bonding Induces One-Dimensional Physics in Bulk Crystal Bilr₄Se₈

Connor J. Pollak, Grigorii Skorupskii, Martin Gutierrez-Amigo, Ratnadwip Singha, Joseph W. Stiles, Franziska Kamm, Florian Pielnhofer, N. P. Ong, Ion Errea, Maia G. Vergniory, and Leslie M. Schoop*



Cite This: J. Am. Chem. Soc. 2024, 146, 6784-6795



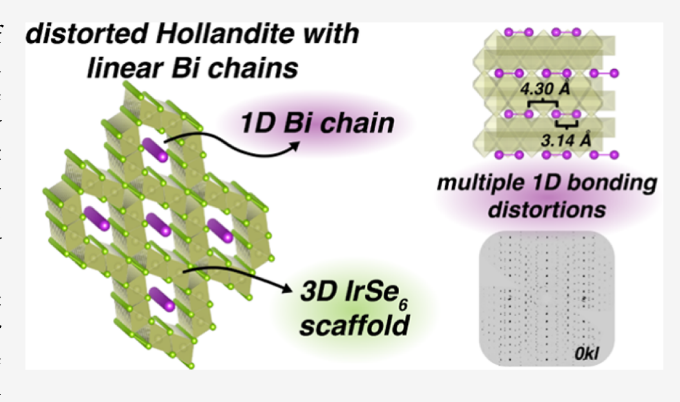
ACCESS

Metrics & More

Article Recommendations

s Supporting Information

ABSTRACT: One-dimensional (1D) systems persist as some of the most interesting because of the rich physics that emerges from constrained degrees of freedom. A desirable route to harness the properties therein is to grow bulk single crystals of a physically three-dimensional (3D) but electronically 1D compound. Most bulk compounds which approach the electronic 1D limit still field interactions across the other two crystallographic directions and, consequently, deviate from the 1D models. In this paper, we lay out chemical concepts to realize the physics of 1D models in 3D crystals. These are based on both structural and electronic arguments. We present BiIr₄Se₈, a bulk crystal consisting of linear Bi²⁺ chains within a scaffolding of IrSe₆ octahedra, as a prime example. Through crystal structure analysis, density functional



theory calculations, X-ray diffraction, and physical property measurements, we demonstrate the unique 1D electronic configuration in BiIr₄Se₈. This configuration at ambient temperature is a gapped Su-Schriefer-Heeger system, generated by way of a canonical Peierls distortion involving Bi dimerization that relieves instabilities in a 1D metallic state. At 190 K, an additional 1D charge density wave distortion emerges, which affects the Peierls distortion. The experimental evidence validates our design principles and distinguishes BiIr₄Se₈ among other quasi-1D bulk compounds. We thus show that it is possible to realize unique electronically 1D materials applying chemical concepts.

■ INTRODUCTION

As the ground states of solid materials are described by complex many-body Hamiltonians, it is often impossible to correctly predict their properties. However, reducing the system to one dimension allows for the exact solutions of certain Hamiltonians. As a result, many exotic physical properties of solids have been predicted in one-dimensional (1D) systems. Examples of interesting phases predicted to appear in 1D extended solids include the 1D S = 1 Haldane chain, which features entangled particles at either end; Majorana Fermions,² sought-after particles which are their own antiparticle that could revolutionize quantum computing; Luttinger liquids,³ the only well understood example of an electron bath that deviates from Fermi liquid behavior; and solitons, localized electronic states that can travel through solids with minimal resistance. Some of these examples involve the fractionalization of an electron, where its spin and charge degrees of freedom are separated. Realizations of solids with such phenomena could lead to the design of computer chips from electrically insulating materials that conduct heat and spin information like metals, potentially solving the problem of resistive heating in transistors.

However, synthesizing and handling true 1D materials is challenging. Different approaches have been taken, although few have had uniform success. Carbon-based systems, like polymers or carbon nanotubes, can have 1D chemical connectivity and properties accordingly, but their overall disorder and lack of crystallinity make them difficult to study, especially in devices that extend beyond a single 1D strand. Another approach is to fabricate nanodevices. Some 1D models have been realized in twisted bilayers of $WTe_2^{\ \ \ \ }$ or assembled Fe chains on the surface of Pb. The fabrication of such devices is laborious, and these types of systems are accordingly low in number.

Ideally, we would be able to make three-dimensional (3D) crystals that harbor 1D physics and thus capitalize on bulk crystals' relative synthetic ease to create scalable structures. This idea has certainly been around for a while, but most

Received: December 1, 2023 Revised: February 8, 2024 Accepted: February 9, 2024 Published: March 2, 2024





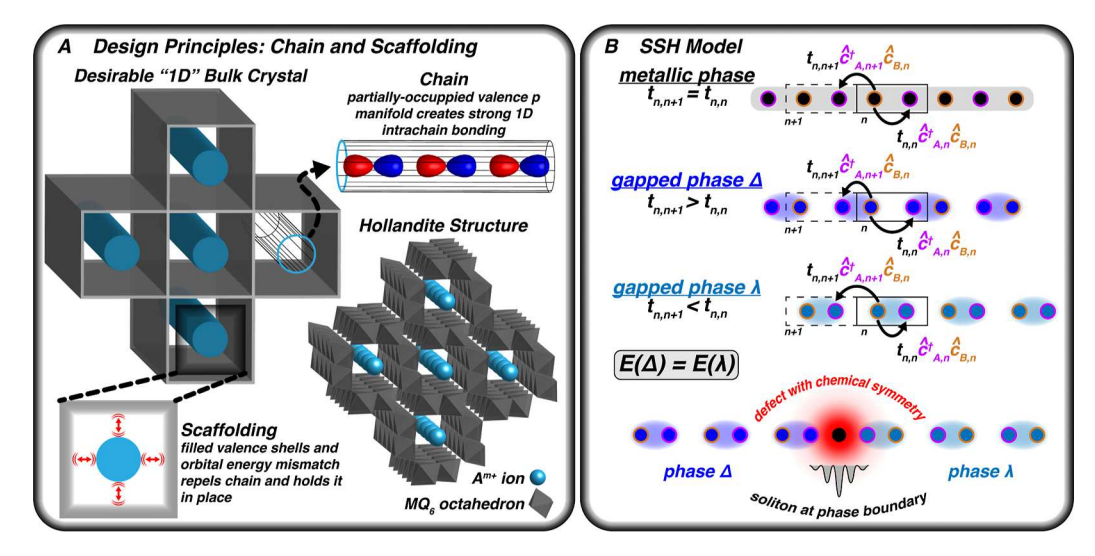


Figure 1. (A) Schematic showing an ideal bulk crystal platform for realization of 1D physics. A rigid scaffolding holds linear chains. The scaffolding situates closed-shell, energy-mismatched species on the tunnel walls to minimize covalent interactions with chains. Chain constituents have partially occupied valence p shells to induce intrachain covalent interactions. The hollandite crystal structure forms a scaffolding from MQ_6 octahedra (M = transition metal, Q = chalcogenide), within which reside 1D chains of A^{m+} ions (m = 1, 2, 3). Crystal structure from ref 17. (B) Demonstration of SSH model. Ideal linear chains may dimerize in one of two degenerate but topologically distinct ways, phase Δ or phase λ . A defect may cause a shift from one phase to the other in a single chain, and the boundary state between phases is a soliton.

crystals with 1D structural motifs exhibit properties that deviate from those of 1D models. Such quasi-1D crystals may possess a measured anisotropy in certain physical properties, a bonding interaction with 1D character,8 or electronic bands dispersed along a single direction in k-space, but never a fully isolated 1D motif with interactions confined to the single dimension. Transition-metal trichalcogenides (MQ_3 ; M = Zr, Nb, Ta; Q = S, Se, Te), transition-metal tetrachalcogenides $[(MSe_4)_n \ I; \ M = Nb, \ Ta], \ molybdenum \ blue \ bronzes$ $(A_{0.3}MoO_3; A = K, Rb, Tl)$, potassium tetracyanoplatinate, organic salts such as tetrathiofulvlene-7,7,8,8-tetracyanoquinodimethane (TTF-TCNQ), and some other inorganic compounds make up the set of canonical quasi-1D bulk compounds that have enjoyed substantial research. 10 Despite the large body of work on such compounds, bulk crystals that display true 1D properties remain scarce.

A couple of design principles outline the chemical logic of a search for such a system (Figure 1A). (1) The system must be separated into two subsystems: 1D chains and scaffolding that holds them in place. Chains are desirable as the 1D geometric motif, as they form the basis for the majority of 1D models. (2) The chain subsystem must have meaningful interactions in 1D. The valence orbitals on the chain ions should be partially filled, incentivizing a bonding interaction. (3) The scaffolding should not interact covalently with the chains. Closed-shell species with an orbital energy mismatch should line the chain-facing walls of the scaffolding. A similar strategy has worked for two-dimensional systems, where a target planar motif has been encapsulated within a noninteractive planar scaffolding to create a bulk crystal with prominent 2D properties. ¹¹

The hollandite crystal structure is the perfect starting point for realizing such a separated environment (Figure 1A). It possesses a 1D scaffolding of edge-sharing metal-chalcogenide octahedra, with chemically isolated ions forming a 1D chain in the tunnels. Typically, the chain consists of alkali, alkaline earth, or lanthanide ions, which do not have unpaired valence electrons. In 2016, a new type of distorted hollandite was introduced, which features Pb²⁺ ions as the chain constituent.¹²

Later, the isostructural analogue $BiIr_4Se_8$ was synthesized, ^{13,14} which formally contains Bi^{2+} ions. Here, the Bi ions in the tunnels are arranged in a linear chain and have a single unpaired electron in the 6p manifold. Thus, $BiIr_4Se_8$ is a bulk crystal uniquely suited to possess 1D physics templated by porbitals at the Fermi level, which feature stronger interactions than the d-orbitals at the Fermi level in many other quasi-1D crystals.

To highlight the implications of the electronic arrangement in $\operatorname{BiIr}_4\operatorname{Se}_8$, we briefly explain the Su-Schrieffer-Heeger (SSH) model. It is the simplest model to describe a topological system in crystalline solids and has been employed successfully to explain drastic swings in polyacetylene conductivity as a function of defect concentration. In the model, electrons occupy sites and hop between them. Within a tight-binding approximation, these sites are valence atomic orbitals. These sites are arranged linearly and grouped into two per unit cell. The sole action available to an electron is to hop between sites, either to the alternate site within the same unit cell or to the alternate site in the adjacent unit cell. The Hamiltonian is $\hat{H} = \sum_{n=1}^N t_{n,n} (\hat{c}_{A,n}^\dagger \hat{c}_{B,n} + \text{H. C.}) \qquad \text{, where H.C. is the}$

+
$$\sum_{n=1}^{N} t_{n,n+1} (\hat{c}_{A,n+1}^{\dagger} \hat{c}_{B,n} + \text{H. C.})$$

hermitian conjugate, N is the number of unit cells, and A and B are different sites. A hop from one site to another within the $n^{\rm th}$ unit cell is represented by a term in the Hamiltonian of the form $(t_{n,n}\hat{c}_{A,n}^{\dagger}\hat{c}_{B,n})$, where $\hat{c}_{B,n}$ annihilates an electron at site B (Figure 1B, orange), $\hat{c}_{A,n}^{\dagger}$ creates an electron at site A (Figure 1B, purple), and $t_{n,n}$ is the so-called "hopping integral", which modulates the probability of a given hop. All of the chemistry is wrapped up in $t_{n,n}$. The hopping integral scales as the overlap integral between the sites, and so two atoms with a covalent chemical bond between them will yield a large hopping integral, whereas two atoms with minimal covalent interactions will have a small hopping integral.

For a system of equally spaced sites, all hops are equally likely, and the SSH model predicts a metallic band structure.

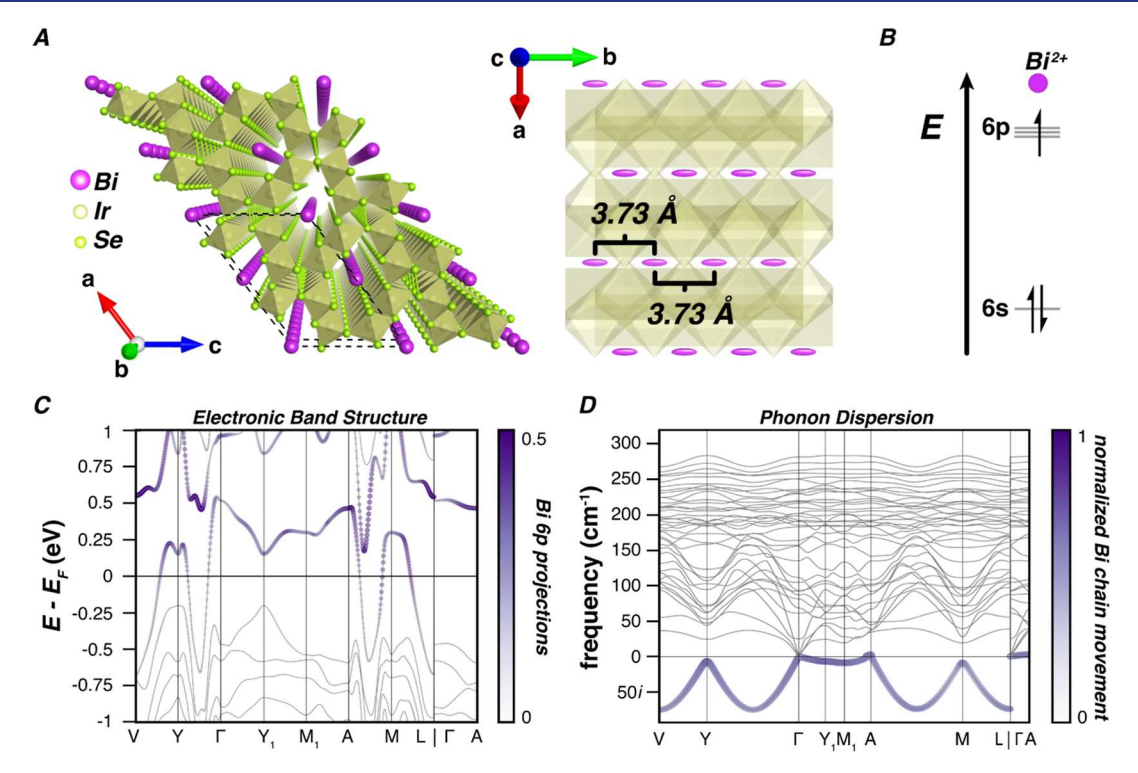


Figure 2. HSS analysis. (A) High-symmetry crystal structure, confirmed via Mo K α X-ray diffraction, showing the 50% probability ellipsoids for equally spaced Bi atoms (purple) residing within scaffolds of iridium (yellow) selenide (green) octahedra. (B) Simple atomic orbital scheme for Bi²⁺ showing the single unpaired electron in the 6p manifold, above the relativistically stabilized 6s state. (C) HSS band diagram with spin—orbit coupling correction, with bands colored according to their Bi 6p atomic states projection. A single band with significant Bi 6p contributions crosses the Fermi level at multiple points in the Brillouin zone. (D) Phonon calculations for the HSS, with each band colored according to the normalized contribution of Bi movement in the chain direction. The plot shows a phonon branch with complex frequency for the majority of the sampled k-path.

Alternatively, a system dimerized into pairs has two types of hops. One is to the adjacent site that is chemically bonded to the current site and has a large t, and the other is to the site in the adjacent dimer and has a small t (in Figure 1B, $t_{n,n+1} > t_{n,n}$ for gapped phase Δ). Here, the SSH model predicts two degenerate but topologically distinct insulating band structures, determined by whether the inter- or intraunit cell hopping has the larger t (phase Δ and phase λ in Figure 1B). In a dimerized, defect-free system, only one of these electronic phases is present in the bulk. 18 In systems with defects, the situation changes. If the defect commands chemical symmetry from the surrounding environment, the chains on either side of the defect will look the same. This switched the electronic state and the corresponding topological invariance class. There must be continuity, however. Consequently, at the boundary between these two topologically distinct electronic states there exists a midgap solitonic state, in direct analogy to the gapless surface states in a topological insulator. This soliton has a very small energy barrier for movement along the chain. More defects means more solitons, and this explains the defectdependent conductivity in polyacetylene. In the SSH model specifically, the formation of a chemical bond, the dimerization of the linear chain, is crucial to the development of solitonderived physics. This bond is formulated in physics terms as a Peierls distortion. The generalized version of this has a wavevector with nonzero components along three reciprocal lattice vectors and is often called a charge density wave (CDW). Here, some combination of Fermi surface nesting and electron-phonon coupling (i.e., chemical bonding) rearranges the crystal lattice and stabilizes the structure. 19

It will be demonstrated here, through crystal structure analysis, electronic structure calculations, experimental diffraction, and physical property measurements, that the Bi chains in BiIr₄Se₈ are largely decoupled from the rest of the crystal lattice and that nontrivial chemical interactions in the Bi chain both template an SSH system via a Peierls distortion and result in further CDW distortions. The evidence presented makes a compelling case that the system fits the chain and scaffolding description better than other bulk systems.

■ RESULTS AND DISCUSSION

High-Symmetry Structural Analysis. The published high-symmetry structures $(HSS)^{13,14}$ for $BiIr_4Se_8$ are in monoclinic spacegroup C2/m (number 12). Bi atoms are equally spaced 3.7 Å apart in linear chains within large tunnels made of zigzag edge-sharing double chains of $IrSe_6$ octahedra (Figure 2A). The tunnels and Bi chains run collinear with the crystallographic b-axis. Running parallel to the major tunnel is a minor tunnel, across which spans a perselenide bond. X-ray photoelectron spectroscopy confirms the perselenide motif (Figure S1).

Electron counting initiates uncertainty regarding the evenly distributed Bi chain structure. The crystal features three important bonding motifs: $(Se_2)^{2-}$ perselenide bonds, distorted IrSe₆ octahedra, and Bi chains. Of the eight Se atoms per formula unit, two are in a perselenide motif and six occupy the typical 2- oxidation state. As well, BiIr₄Se₈ is measured to be diamagnetic, ¹³ and so the four Ir atoms must be in the low-spin d⁶ 3+ configuration. To balance charge, Bi must occupy a formal oxidation state of 2+. This is uncommon

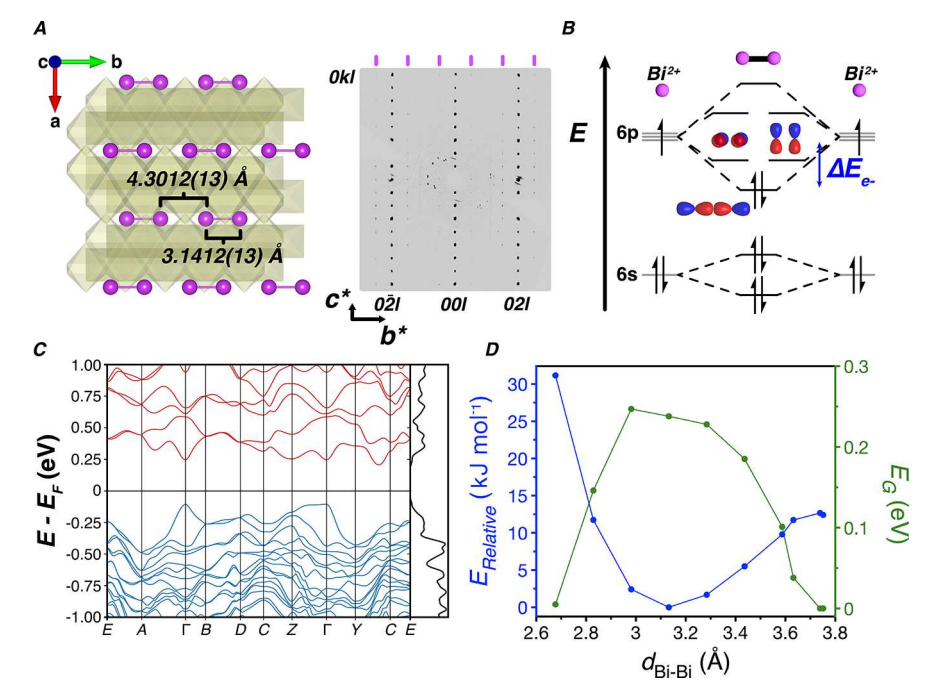


Figure 3. Peierls distorted structure. (A) Structural model (left) from a commensurately modulated solution with spacegroup P2/n showing Bi atoms grouped into dimers, each with a bond length of 3.18 Å. Synthesized precession image in the 0kl plane (right), where the purple ticks correspond to columns of Bragg peaks at $q_1 = 0.5b^*$; (B) simple orbital model showing the chemical incentive for Bi bond formation (radial nodes are omitted for clarity); (C) SOC-corrected band structure for the dimerized structure, showing an energy gap at the Fermi level with occupied bands in blue and unoccupied bands in red, and a relative density of states on the right; and (D) relative configuration energy vs Bi–Bi dimerization coordinate (left axis, blue) and corresponding bandgap vs dimerization coordinate (right axis, green).

as it leaves a single electron unpaired in a high-energy 6p orbital (Figure 2B). Nevertheless, this assignment is supported by the existence of the isostructural Pb analogue. 12 In the Bi analogue, then, some bonding interaction that works to stabilize the Bi 6p states should occur. The most reasonable prediction is the arrangement of adjacent Bi atoms into $(Bi_2)^{4+}$ dimers, a motif permitted by the geometry of the crystal structure and which has literature precedent. $^{20-22}$ This interaction is not captured in the HSS. Such dimerization would enable the simple SSH model in this system.

Interestingly, the high-symmetry crystallographic model itself hints at its incompleteness. Acceptable residual electron density only arises when one invokes either anisotropic disorder parameters (ADPs) along the chain direction or multiple partial-occupancy Bi sites. ^{13,14} At room temperature, our own single-crystal X-ray diffraction measurements confirm the aberrant thermal ellipsoids (Figure 2A). The size of the thermal ellipsoids and their alignment along the chain direction are possible indications of an order not yet captured, such as that of a (Bi₂)⁴⁺ dimerization.

Density functional theory (DFT) calculations using the Perdew–Burke–Ernzerhof (PBE) functional²³ predict the HSS of BiIr₄Se₈ to be metallic with a single band crossing the Fermi level (Figure 2C, k-vector types in Figure S17A). Calculations with the modified Becke-Johnson (mBJ) functional²⁴ yield largely the same band structure (Figure S6). States crossing the Fermi level field make significant contributions from Bi 6p orbitals (Figure 2C). Other orbitals, Ir 5d and Se 4p, also contribute to the metallic band (Figure S2), but further analysis implicates Bi chains as the source of metallicity. The high-symmetry lines in k-space that run along the chain, V-Y, $Y-\Gamma$, A-M, and M-L, show highly dispersed bands. High-symmetry lines perpendicular to the chain

direction, $\Gamma - A$, $Y_1 - M_1$, and the not shown Y - M, show significantly less dispersed bands. As well, electron localization function (ELF) calculations show the Bi chains to be settled in a near-constant ELF, which approaches the value expected for an electron gas, whereas Ir and Se possess significantly more localized states (Figure S3A,B). Finally, constant energy cuts in the k-space from -200 to 200 meV (with $E_F = 0$) manifest as two distorted flat sheets oriented perpendicular to the Bi chain direction (Figure S4). Viewed at a coarse level, the wavevector component along the chain direction is the sole variable which determines the energy of a given state in the metallic band. The sum of all this information indicates that the metallic band is of significant Bi chain character, with little chemical mixing between chain and scaffolding. Thus, the electronic system of the HSS is highly 1D near the Fermi level. While not identical, this situation is similar to that predicted for a regularly spaced, metallic 1D chain, the canonical host to the Peierls instability.²⁵ In BiIr₄Se₈, as in the idealized chain, a wavevector of $q = 0.5b^*$ nests the Fermi surface (Figure S5) and creates an instability toward a distortion that doubles the unit cell along the chain direction.

Phonon calculations are useful tools to test whether a crystal structure is stable. Shown in Figure 2D is the phonon dispersion relation calculated for the HSS of BiIr₄Se₈. Strikingly, there exists a branch of the phonon spectrum that has a complex frequency for the majority of the sampled k-path, clearly showing that the HSS is unstable. All modes in this branch are dominated by the Bi movement along the chain direction (Figures 2D and S8). Thus, the metallic system of equally spaced Bi atoms in the HSS is unstable to myriad possible distortions that all, in one way or another, group Bi atoms together in an extended bonding interaction. The most relevant of these distortions to both the chemical bonding

picture of Bi dimerization and the Fermi surface nesting picture is the aforementioned $q = 0.5b^*$. A group theoretical analysis of the symmetry reduction from a distortion with this wavevector is given in the Supporting Information.

In addition to demonstrating an energetic incentive for intrachain Bi bonding, the phonon spectrum provides evidence that Bi chains may be thought of as individual 1D units isolated from the surrounding Ir–Se scaffolding. At both the Γ -point and the A-point, the phonon modes associated with the complex-frequency branch have positive but near-negligible frequencies of 0.5 and 2.7 cm⁻¹, respectively (Figure 2D). As with the rest of the branch, the atomic displacements of the modes on the Γ -A line are dominated by the movement of Bi along the chain direction (Figure S9). Because wavevectors on the Γ -A line are perpendicular to the chain, the Bi displacements within a single chain from modes along this line are equal in amplitude and in-phase, corresponding to coherent sliding of Bi chains along the inside of the tunnels. At room temperature, ambient thermal energy is far above that of the modes from the Γ -A line and likely far above activation barriers to shift the position of any given Bi chain within the crystal coherently along the tunnel. This is a strong indication that chains are decoupled from the rest of the crystal lattice and that BiIr₄Se₈ approaches the conception of chains within a noninteracting scaffolding.

With all of this in mind, it is puzzling that a distortion has not yet been observed 13,14 when such a dimerization should have a stark effect on the crystal structure. This implies that it may not be easily visible on first glance in diffraction, that more could be happening than a simple, rigid bond formation. We therefore next perform experimental characterization on ${\rm BiIr_4Se_8}$ single crystals, paying close attention for potentially subtle signatures of a distortion.

EVIDENCE OF PEIERLS STATE

The most important experimental indication of a Peierls distortion would be a doubling of the HSS unit cell along the chain direction in accordance with the instabilities demonstrated for $q = 0.5b^*$. Close examination of diffraction patterns of BiIr₄Se₈ from laboratory instruments with Mo Kα radiation reveals weak but coherent superlattice Bragg peaks at q_1 = $0.5b^*$ at room temperature (Figure 3A, right; purple ticks). Bi and Ir are strong X-ray absorbers at Mo K α wavelengths, and this makes the peaks easy to miss. We also measured diffraction at a synchrotron using 30 keV radiation. Measurements at room temperature show the $q_1 = 0.5b^*$ satellite intensities to be roughly 4 orders of magnitude weaker than the main reflections, with no apparent reflection conditions. Thus, at room temperature, the doubling distortion is a weak but noninsignificant perturbation on the underlying charge density, as expected in the context of a clear Peierls distortion.

Cooling to 100 K on the Mo source yielded $q_1 = 0.5b^*$ reflection intensities significant enough to permit a commensurately modulated structure solution for the q_1 peaks. This solution shows the doubled unit cell resulting from a Bi-Bi dimerization. Various reasonable structural models exist, each of which results in a slightly different Bi-Bi distance and dimer location within the tunnel. The model that best reflects the results discussed previously is in SG P2/n (SG 13) and has chains with Bi-Bi dimers of 3.18 Å. This is over 0.5 Å shorter than the same distance in the HSS, nearly a 16% contraction (Figure 3A, left). This is different from most other "Peierls distortions" in quasi-1D compounds. In NbSe₃, the Nb atoms

are grouped loosely into tetramers with an approximate amplitude of 0.05 Å. 26 (TaSe₄)₂ I sees Ta atoms shift with an amplitude of 0.025 Å into one, two, and three atom clusters.²⁷ TaTe₄ and NbTe₄ see large metal movements of approximately 0.3 Å into approximate triplets, while the surrounding Te atoms shift around it. 28,29 The CDW in K_{0.3}MoO₃ moves the Mo atoms in a staggered fashion transverse to the 1D direction with an amplitude of 0.04 Å.30 The CDW in TTF-TCNQ principally shifts the whole TTF molecule approximately 0.02 Å.31 Thus, the simple, porbital-based Bi dimerization of more than 0.5 Å amplitude is structurally unique among quasi-1D compounds. In the dimerized crystallographic model, Bi still has elongated ADPs directing along the chain direction. As well, letting Bi occupancy freely refine leads to an empirical formula unit of Bi_{0.88}Ir₄Se₈ (Table S2). Such a drastic reduction in occupancy is likely an artifact of observed electronic disorder along the Bi chain and not an indication of actual crystal composition. This observed disorder and the elongated ADPs could be a sign of another uncaptured order in the Bi chain (discussed later). Nevertheless, Bi vacancies remain a possibility that could impact electronic properties by creating soliton boundary states, for example.

Since the q_1 -peaks carry information about Bi–Bi dimerization at 100 K, their presence at room temperature indicates that the dimerized CDW structure is the room temperature ground state. Further structural evidence for Bi dimers at room temperature comes from Raman spectroscopy (Figures S12 and S13), where a peak appears at the frequency predicted for a Bi–Bi dimer. This frequency agrees with the literature precedent for $(\mathrm{Bi}_2)^{4+}$ motifs. $^{20-22}$

If the conception of canonical Peierls distortion holds true in BiIr₄Se₈, the dimerization should open a bandgap in the energy spectrum. This is exactly what is computed in band structure calculations, which predict the dimerized structure of BiIr₄Se₈ to be a small bandgap indirect semiconductor with bandgap E_C = 311 meV (Figure 3C, k-vector types in Figure S17B). Spin orbit coupling (SOC) was included in the calculation. We expect this dimerized band structure to be more isotropic than that of the HSS as the system distorts away from the 1D instability. What results from this dimerization, however, is a system with the prerequisite geometry to host 1D soliton physics at the boundary of these dimerized states. To demonstrate the stabilization mechanism, we next systematically vary the Bi-Bi bond length in non-SOC DFT calculations and track the resulting energy and bandgap. The most stable structure occurs when the Bi-Bi distance is between 3.1 and 3.2 Å, with a bandgap of roughly 230 meV (Figure 3D). This distance agrees well with the experimentally determined bond distance. As SOC was neglected in the latter calculations, the bandgaps will be less accurate.

The predicted semiconducting ground state can be easily confirmed by measuring the temperature-dependent electrical resistivity of single crystals, $\rho(T)$ (the conductivity is $\sigma=1/\rho$). From 300 to approximately 200 K, BiIr₄Se₈ is semiconducting (Figure 4A) and follows an Arrhenius temperature dependence with a transport barrier of 146 meV (Figure 4B). Transport activation energies vary batch-to-batch between 80 and 170 meV, the variation likely a result of midgap impurity state electronic transport. The origin of these impurity states is unknown, though Se vacancies or oxygen impurities are possibilities. The transport activation energy is direct experimental evidence that supports the assertion of a Peierls

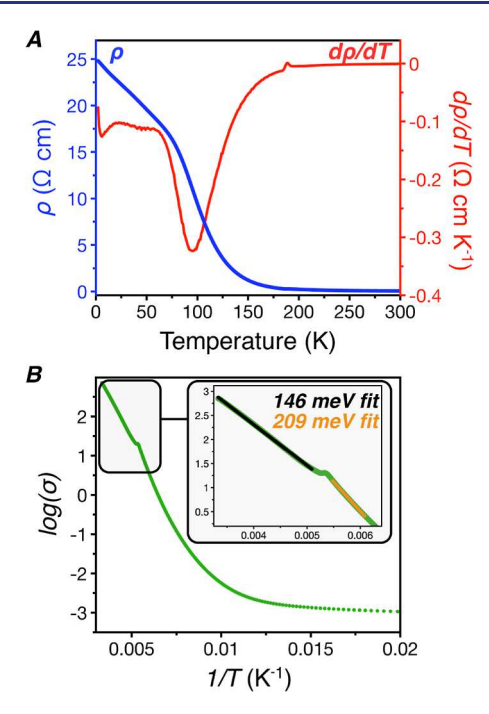


Figure 4. Longitudinal resistivity and Arrhenius plot. (A) Typical resistivity vs temperature (blue, left axis) and its corresponding derivative (red, right axis). (B) Arrhenius plot (green) of $\log(\sigma)$ vs 1/ $T(\sigma = 1/\rho)$ between 300 and 50 K, with an inset showing linear fits from 300 to 190 K (black) corresponding to a 146 meV barrier and 183-163 K (orange) corresponding to a 209 meV barrier.

distortion in BiIr₄Se₈ and confirms the computational predictions presented above.

Though not the focus of this paper, it is worth mentioning that the resistivity does not behave as expected for a regular semiconductor, as it does not diverge at low temperatures but saturates. There are many possible causes for this, including a physical metallic inversion layer on the surface, ^{33,34} a physical impurity phase due to the dynamics of flux crystal growth, a topologically nontrivial metallic surface state, 35 some combination of these, or a wholly different mechanism. Further investigation to understand the nature of this conduction pathway is ongoing.

Incommensurate CDW at 190 K. The resistivity profile at intermediate temperatures hints at an additional distortion. The red derivative plot in Figure 4A shows an anomaly at approximately 190 K. It exists as a 5 K window where the resistivity levels off with decreasing temperature. After this window, decreasing temperature again sees increasing resistivity, though now in a non-Arrhenius manner (Figure 4B). This feature is almost totally invariant to magnetic fields up to 9 T, and it exhibits thermal hysteresis (Figure 5A,B). Importantly, at temperatures immediately below the transition, the slope of $log(\sigma)$ vs 1/T is near-linear, though it is now steeper than that just above the transition temperature with a fitted barrier of 209 meV (Figure 4B). This indicates that the bandgap increases across this temperature window. Because BiIr₄Se₈ already has a bandgap above the transition temperature, carrier concentration should change little across the transition, and the conductivity increase at 190 K is likely derived from changing carrier mobilities.

In Hall measurements, as temperature sweeps high to low from 195 to 170 K across the transition, the dominant carrier type switches from electrons to holes at the onset of the transition and then back to electrons below (Figure 5C). Clearly, some rearrangement of the electronic structure occurs here. Heat capacity measurements also show a feature at the same temperature (Figure 5D). Thus, an electronic distortion

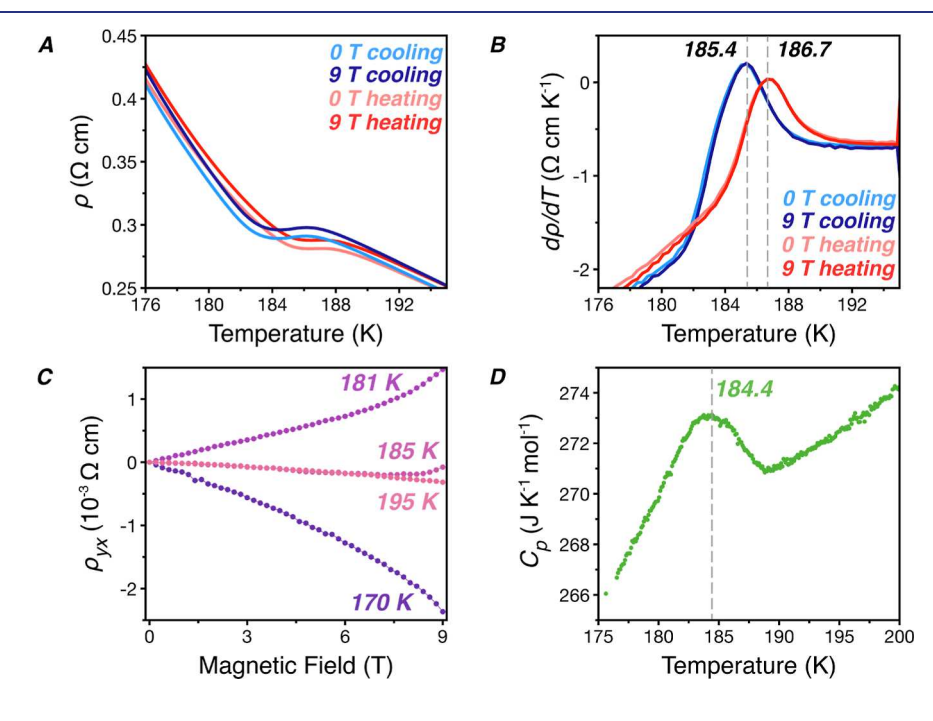


Figure 5. Physical property anomalies at 190 K. (A) Resistivity versus temperature curves at different applied magnetic fields. Cooling at 0 T (light blue) and 9 T (dark blue) and heating at 0 T (pink) and 9 T (red). Applied magnetic field makes little modification to the temperature profiles. Thermal hysteresis in the feature is evident at both field values. (B) Derivative plots of the resistivity curves from (A) demonstrating thermal hysteresis and invariance to applied fields up to 9 T. (C) Hall resistivity for four temperatures that span the transition showing a slope change for the two temperatures within the transition. (D) Heat capacity shows a peak at the transition temperature.

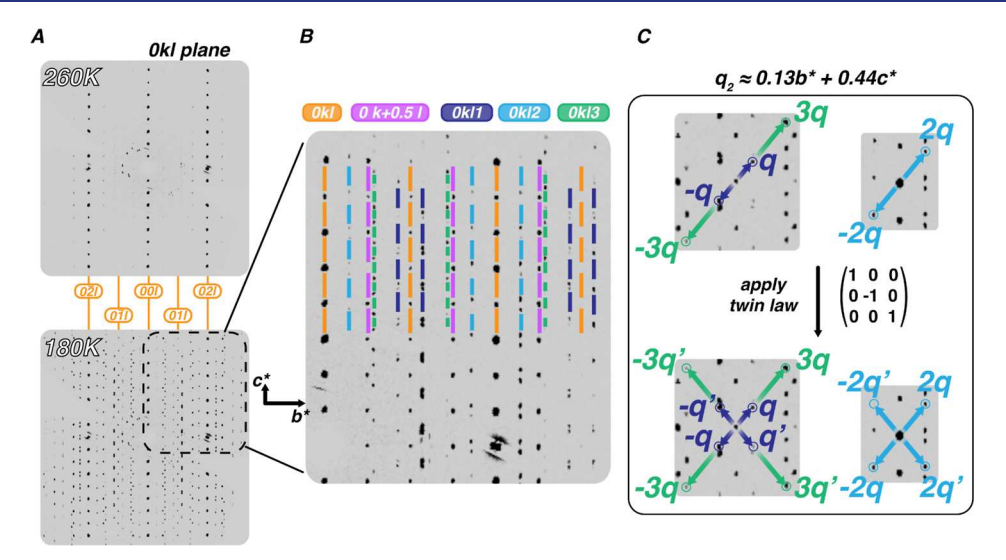


Figure 6. Indexing the complex X-ray diffraction pattern. (A) Synthesized precession images in the 0kl plane of the C2/m high-symmetry cell at 260 and 180 K, with indexed 0kl column locations shown in orange. (B) Indexed upper right quadrant of the 0kl plane at 180 K showing columns of main reflections in orange, Peierls q_1 reflections in pink, first-order q_2 -vectors in dark blue, second-order q_2 -vectors in turquoise, and third-order q_2 -vectors in green. (C) q_2 -vectors and harmonics are shown in relation to the associated main reflection. The reflection condition on q_2 -peaks h + k + m = 0 is evident here. A mirror twin operation is required for a complete indexing of the reflections.

occurs at 190 K which creates a larger bandgap, shuffles the identity of the valence band, and carries an entropic signature. Such property signatures often accompany the transition to a CDW state. We next present temperature-dependent synchrotron single-crystal diffraction measurements that confirm the presence of a second periodic charge distortion.

Cooling to below 200 K, where the anomalies in property measurements occur, introduces complexity to the symmetries observed in the Bragg peaks. The precession images at 180 K explode in off-integer complexity (Figure 6A). Superlattice reflections appear at noninteger multiples of HSS reciprocal lattice vectors. Even with these distortions occurring, the main reflections from the high-symmetry cell remain largely unaltered. The Peierls peaks are also qualitatively unaltered, and the associated q-vector remains $q_1 = 0.5b^*$. When viewed at a coarse level, the dominant underlying charge density remains unchanged.

The complex pattern of reflections may be indexed with integers hklm to explain every observed peak (Figure 6B). Below 200 K, in addition to the Peierls distortion, an incommensurate q-vector is present that has nonzero coordinates for two reciprocal lattice vectors: $q_2 \approx 0.13b^* +$ $0.44c^*$. A reflection condition of (h + k + m) = 2n is observed for the q_2 -peaks and is evident in a comparison between the 0kland 1kl planes (Figure S14). This reflection condition indicates that the superlattice peaks are from a modulation and not some physical deformity of the crystal. Additionally, the reflection condition on q_2 -peaks is evidence that the q_1 Peierls distortion at room temperature is not a full structural phase but rather a modulation. This is because the incommensurate reflection condition makes sense only if the unit cell is undoubled along the b direction. This implies that the undoubled HSS is the host of the instability that induces the incommensurate qvector, not the doubled Peierls cell, despite the fact that the Peierls q_1 distortion is present at the critical temperature for the incommensurate q_2 -vector.

To properly index the pattern, either the invocation of a mirror twin domain (Figure 6C) or another q_2 -vector related by a sign flip of either the b^* or c^* component is required. In

distorting from the HSS to any dimerized structure, a mirror plane symmetry element is broken. This could be the source of this twin domain. For reference, in the quasi-1D compound TTF-TCNQ, both situations, a mirror twin or two *q*-vectors, are true at different temperatures.³⁶

The actual real-space effects of the modulation are not yet understood. It is possible that the modulation involves Ir movement through octahedra edges. Nevertheless, because Ir thermal ellipsoids are small in the 100 K structure and the Bi ADPs are large and oriented along the chain, the distortion is likely another Bi—Bi interaction.

When the intensities of different types of peaks are tracked with temperature, a highly unusual feature of both distortions is revealed. Shown in Figure 7 are peak intensities from a set of reflections from the same crystal tracked from 100 to 260 K, normalized first to the intensities of a consistent set of main reflections and then to the intensity of these peaks, or regions in reciprocal space they occupy, at 260 K.

As seen in Figure 7, on moving from high temperature to low temperature, all orders of q_2 -peaks initiate an intensity increase at 190 K. The q2-peak intensities rise until 175 K, where they reach a maximum. For the first-order peaks, this rise is precipitous, topping out at nearly 500× the intensity before the transition. With further cooling, all three types of q_2 peaks decrease in relative intensity dramatically. This contrasts with the temperature dependence outlined by the weak coupling BCS limit, where the *q*-peak intensity should rise and then saturate asymptotically with further cooling. In thusdiscovered quasi-1D compounds, some form of monotonically increasing intensity dependence with cooling is quite general.^{37,38} Canonical quasi-1D compounds NbSe₃,³⁹ (TaSe₄)₂ I,⁴⁰ K_{0.3}MoO₃,⁴¹ and TTF-TCNQ,⁴² all experience the sigmoidal rise in intensity characteristic of the weakcoupling BCS theory. Other members of the quasi-1D family invariably have some type of monotonic increase. 43-49 BiIr₄Se₈ is then unique among quasi-1D compounds.

The temperature dependence of the Peierls distortion q_1 -peaks (pink) follows nearly the exact trend in intensity as the q_2 -peaks, indicating that the Peierls distortion is affected in

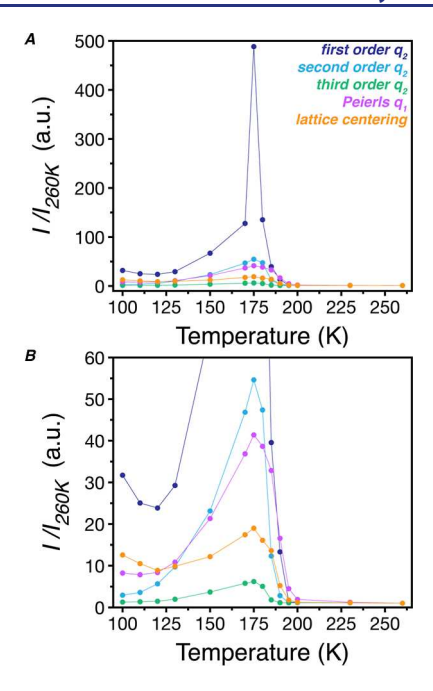


Figure 7. Noncanonical variation of intensity with temperature for different types of reflections. (A) Full data set and (B) same data, with different axis scales. First-order q_2 -peaks are dark blue, second-order q_2 -peaks are turquoise, third-order q_2 -peaks are green, Peierls q_1 -peaks are pink, and peaks associated with C-centering reflection conditions are orange. Intensities for a consistent set of reflections are normalized systematically to both a consistent set of main reflections and the intensity for that region in diffraction space at 260 K.

some way by the incommensurate q_2 -vector despite the fact that there are no observed mixed peaks. Also, peaks associated with lattice centering reflection conditions h + k = 2n for the high-symmetry cell in SG C2/m (Figure 7, orange) follow a similar intensity trend as q_2 -peaks, reflecting the deviation of the electron density from the C-centered HSS.

The qualitative nature of the q_2 Bragg reflections also holds information about the ordering (Figure 8A). Above the

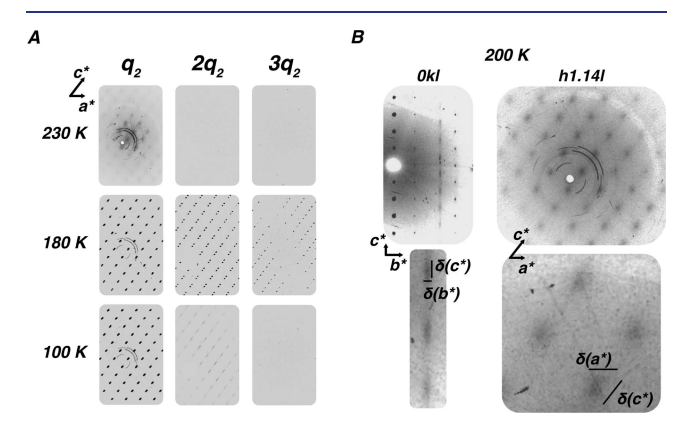


Figure 8. Bragg peaks as a function of temperature. (A) Temperature progression for first-, second-, and third-order q_2 -peaks. At 230 K, diffuse scattering is present at first-order positions. At 180 K, three orders of q_2 -peaks are present. At 100 K, first-order peaks are present, second-order peaks are streaked along the c^* direction, and third-order peaks are absent. (B) Diffuse scattering at 200 K. 0kl plane (left) and h1.14l plane (right) showing diffuse scattering. Rough characteristic peak widths along each reciprocal lattice direction, $\delta(a^*)$, $\delta(b^*)$, $\delta(c^*)$ are shown. $\delta(b^*)$ < $\delta(a^*)$ $\simeq \delta(c^*)$.

incommensurate transition at 230 K, diffuse scattering blotches appear centered at the locations where first-order Bragg peaks will later form. Here, local correlations begin to condense, but long-range order is not yet present. Notably, the shape of the diffuse scattering spots indicates that the correlation length is longer along the chain direction than either direction transverse to it (Figure 8B). This is a strong indication that the ordering induced by the CDW is predominantly 1D, oriented along the crystallographic b-axis. Just below the incommensurate transition at approximately 190 K, first-, second-, and third-order q_2 -peaks condense into sharp reflections. Correspondingly, the modulation functions are complicated and nonsinusoidal. As the temperature decreases further, the periodicity of the CDW remains the same (aside from minor changes to the q_2 -vector itself), but the amplitudes of the peaks diminish. At 100 K, the first-order q_2 -peaks are coherent reflections, but the second-order peaks have been smeared out along the c^* direction, and the third-order peaks are not observed. This state of periodicity, a simplified and sinusoidal q_2 ordering, is maintained down to 10 K (Figure S15).

One possible reason for the noncanonical q-peak temperature dependence is the formation of numerous CDW domains around local defects. The real-space location of an incommensurate CDW within the crystal is influenced by an energy landscape determined by both the average crystal structure and the local defects. These defects create minima in this energy landscape that can be pinned by the CDW to a specific position. Just below the q_2 transition, the relatively abundant thermal energy may allow the newly formed CDWs to overcome this pinning—the CDW exists as a coherent domain with a definite phase relationship, leading to intense scattering. With cooling, the ability to overcome pinning is reduced, and CDWs increasingly lock in to local domains with random phase relationships. As more of these distinct scattering domains form, they lead to a decrease in the observed Bragg peak intensity.

Another possibility for the temperature dependence is competing order. ⁵⁰ In this competition, the increase in magnitude of a certain order parameter, e.g., a magnetic ordering vector, comes at the direct expense of the magnitude of an existing order parameter, like a charge ordering. It is possible that in $BiIr_4Se_8$, the intensity vs temperature profile of the incommensurate q_2 -peaks comes from such a parasitic relationship, that the intensity drop below 175 K is siphoned into an ordering process elsewhere in phase space.

CONCLUSIONS

Using chemical logic, we pointed out that $BiIr_4Se_8$ is an extraordinary 1D compound that hosts linear chains of chemically bonded Bi atoms in a scaffolding of Ir–Se octahedra. The involvement of p orbitals in a 1D chain distinguishes $BiIr_4Se_8$ from other quasi-1D compounds, which involve weaker interactions of d orbitals, making it a perfect candidate to probe 1D physics in a 3D crystal. We highlighted the instability in the reported HSS and showed via phonon calculations that the chain and scaffolding on $BiIr_4Se_8$ are mostly decoupled. High-resolution diffraction confirms the presence of a Peierls distortion already at room temperature. Still, the supercell diffraction spots are weaker than expected for a commensurate doubling of the unit cell, pointing to unusual disorder in the dimerization, such as small domains.

We further revealed an additional structural rearrangement below 190 K, which is evident in transport, specific heat, and diffraction. We provided evidence that this second CDW is linked to the Peierls distortion. The temperature dependence of superlattice peak intensities indicates a deviation from the body of quasi-1D compounds thus studied and further suggests unusual lattice rearrangements in BiIr₄Se₈. If a CDW locks in to a single domain below a certain temperature, changes in the reflection intensities are not expected upon cooling as the thermal vibrations of atoms decrease. Thus, our result indicates that simple dimerization of Bi2+ will not be sufficient to minimize the system's energy, and consequently, a rich playground of states and physical phenomena are waiting to be explored in this compound.

Initially, particular attention was paid to the SSH model, and subsequently, BiIr₄Se₈ was shown to possess the prerequisite chemistry to apply. Systematic doping studies may be a fruitful avenue for further work. Luckily, the system has a ready mechanism to perform systematic doping in the form of Se vacancies. By varying the Se concentration in the synthesis melt, synthetic control over vacancies may be achieved. Another route is to dope with other transition metals. Pt and Ru are desirable here as a way to introduce electron- or holetype impurities into the system. Se vacancies may be more effective for creating phase boundaries in the SSH system specifically, as the Se atoms are closer to the Bi chains than the transition metals. Finally, the electron count in the Peierls chain could be varied by substituting small amounts of Bi with

To conclude, we here introduced a new 1D system using chemical reasoning and provided initial evidence of rich complex physical phenomena that can be further explored. Thus, BiIr₄Se₈ and its variants (doped or substituted) are likely to stimulate renewed interest in 3D crystals with 1D electronic properties.

EXPERIMENTAL SECTION

Synthesis of Single Crystals. Single crystals were synthesized via a Bi self-flux reaction by placing Bi (652 mg, 99.9%, Sigma-Aldrich), Ir (100 mg, 99.9%, Sigma-Aldrich), and Se (206 mg, 99.99%, Sigma-Aldrich) into a 13 mm diameter alumina crucible in the stoichiometric ratio 6:1:5 and placing into a 16 mm diameter fused silica tube with silica wool placed on top for filtration during centrifugation. The tube was purged with Ar three times and flamesealed under a 67 mTorr Ar backfill. The tube was heated to 1000 °C at 20 °C/h, held at 1000 °C for 24 h, and cooled at a rate of 1.2 °C/h to 800 °C, where it was centrifuged to separate Bi flux from crystals. Crystals are rodlike with a shiny, dark appearance, displaying clean facets. They are often intergrown, with usual thicknesses of 250 μm and lengths of several mm. Crystals are structurally air stable, although prolonged air exposure modifies electronic transport properties.

X-ray Diffraction. Laboratory data was collected on a Bruker X8 Duo with an APEX II CCD detector using Mo K α radiation (λ = 0.71073 Å) with a graphite monochromator. Temperature was controlled with a Cryojet N2 stream.

APEXII (Bruker-AXS) was used to determine unit cells and synthesize procession images. Data were integrated, scaled, and corrected for absorption using SADABS (Bruker-AXS). Superflip⁵¹ was used for structure solution, and Jana2020⁵² was used for the fullmatrix least-squares refinement on F^2 of the 100 K structure.

Synchrotron data was collected at Sector 15 ID (NSF's ChemMatCARS) using endstation D. Thirty keV radiation (0.413 Å) was monochromated with a Si(111) crystal. T = 100-300 K data was cooled with a Cryojet N2 stream, and 10 K data was collected with an open-flow liquid He cryostat. Reflections were measured on a

Dectris Pilatus 3 × 1 M CdTe detector. Data workup was performed in ApexIII (Bruker-AXS).

Electronic Transport. Longitudinal and Hall resistivities were measured on a Quantum Design DynaCool PPMS from 1.8 to 300 K and 0-9 T. Crystals were selected, cleaned, and polished. They were attached to a sapphire substrate via GE varnish (GE 7031), and 25 μ m diameter gold wires (99.95%, Thermo Scientific) were attached to the crystal in either a linear four point geometry or a linear hall geometry with conductive silver paint (DuPont 4922N). Contacts were tested with a multimeter. Because the sample is semiconducting, any point-to-point resistance measurement under 10 Ω yields excellent results, though up to 50 Ω (depending on the crystal shape) is viable.

R vs *T* is measured typically with a sweeping temperature ramp of 2 K per minute, though for the hysteresis measurements, temperatures were allowed to equilibrate at each point before resistance measurements were collected. Hall measurements were collected from -9 to 9 T in 1000 Oe steps, and the data were antisymmetrized to extract the Hall component.

Heat Capacity. Heat capacity was measured by using the heat capacity module on a Quantum Design Dynacool PPMS. A small amount of Apiezon N grease was placed on the sample holder, and addenda measurements were performed. Single crystals were selected, cleaned of surface debris, and placed on N grease. Temperature was increased by 2%, and the decay was measured for 2 tau, where tau is

X-ray Photoelectron Spectroscopy. XPS measurements were carried out on a single crystal of BiIr₄Se₈ using a Thermo Scientific K-Alpha XPS system. Sample preparation was done in an argon atmosphere glovebox, and the samples were transferred to the XPS system using a vacuum transfer module to prevent contamination from the air. A 200 μ m X-ray spot size was used on a polished surface of the crystal to eliminate surface contaminants. The Se 3d_{5/2} and 3d_{1/2} peaks were fit using CasaXPS using a Shirley background and symmetric peaks shapes. No appreciable difference in the spectrum is observed after depth profiling with an ion beam.

Raman Spectroscopy. Raman spectra were collected at room temperature on a Horiba Confocal Raman microscope. Samples were ground into a powder and spread across a glass slide. Samples were irradiated with 532 nm radiation. 10× magnification was used, with an intensity filter that halves the strength of the incoming radiation. A confocal hole of 250 μ m was used, along with a spectrometer grating of 2400 g/mm.

First-Principles Calculations. The first-principles DFT calculations of the high-symmetry (nondimerized) phase were conducted using the Quantum Espresso package. 53,54 We used the generalized gradient approximation (GGA) with the PBE parametrization²³ together with projector-augmented wave pseudopotentials generated by Dal Corso⁵⁵ and considering 15/9/16 valence electrons for bismuth/iridium/selenium. We also performed calculations with the mBJ method.²⁴ In all cases, we used an energy cutoff of 70 Ry with a Methfessel-Paxton smearing⁵⁶ of 0.012 Ry. The structural relaxation was performed using a $15 \times 15 \times 6$ k-grid, the experimental lattice parameters, without accounting for SOC and was stopped when forces are below 10^{-5} a.u. Subsequently, SOC was included to compute the electronic band structures. To compute the Fermi surface and ELF, we employed a denser k-grid of $25 \times 25 \times 10$, with the inclusion of SOC for the case of the Fermi surface. Harmonic phonons were computed using density functional perturbation theory⁵⁷ within a $2 \times 2 \times 2$ supercell in the absence of SOC.

All calculations are performed on the primitive version of the HSS, and then reciprocal lattice vectors are translated to those of the centered C2/m cell.

For the low-symmetry (dimerized) phase, we used the same structural relaxation procedure as in the high-symmetry phase using Quantum Espresso and experimental lattice parameters, with the only difference being the use of a $6 \times 6 \times 6$ k-grid. However, for the electronic band structure of the low-symmetry phase, the simulations were performed using the Vienna ab initio simulation package (VASP)^{58,59} and also with projector-augmented wave pseudopotentials. We used an energy cutoff of 500 eV together with an energy threshold of 10^{-7} eV, a $6 \times 6 \times 6$ k-mesh, and the inclusion of SOC. Regarding the pseudopotentials, we used the ones included with VASP, ^{60,61} containing 5, 9, and 6 electrons for Bi, Ir, and Se, respectively.

Non-SOC DFT calculations with varying Bi—Bi bond lengths were performed in the framework of DFT using CRYSTAL17. 62,63 Bi—Bi distances were frozen in, and the rest of the structure was allowed to relax. The PBE exchange—correlation functional of the GGA was used for all calculations. 64 Basis sets for Bi, Ir, and Se were taken from the literature. $^{65-67}$ The convergence criterion considering the energy was set to 1×10^{-8} arbitrary units, and a k-mesh sampling of $6\times 6\times 6$ was used. Vibrational frequencies, including Raman intensities, were computed using the coupled-perturbed Kohn—Sham mode. $^{68-70}$ The Raman spectrum was simulated at room temperature (298 K) with an excitation wavelength of 532 nm.

ASSOCIATED CONTENT

Supporting Information

The Supporting Information is available free of charge at https://pubs.acs.org/doi/10.1021/jacs.3c13535.

Crystallographic model information, band structure calculations, single-crystal diffraction precession images, and property measurements (Raman spectroscopy, X-ray photoemission spectroscopy, heat capacity) (PDF)

Accession Codes

CCDC 2310921 contains the supplementary crystallographic data for this paper. These data can be obtained free of charge via www.ccdc.cam.ac.uk/data_request/cif, or by emailing data_request@ccdc.cam.ac.uk, or by contacting The Cambridge Crystallographic Data Centre, 12 Union Road, Cambridge CB2 1EZ, UK; fax: +44 1223 336033.

AUTHOR INFORMATION

Corresponding Author

Leslie M. Schoop — Department of Chemistry, Princeton University, Princeton, New Jersey 08544, United States; orcid.org/0000-0003-3459-4241; Email: lschoop@princeton.edu

Authors

Connor J. Pollak – Department of Chemistry, Princeton University, Princeton, New Jersey 08544, United States Grigorii Skorupskii – Department of Chemistry, Princeton University, Princeton, New Jersey 08544, United States

Martin Gutierrez-Amigo — Department of Physics, University of the Basque Country (UPV/EHU), Bilbao 48080, Spain; Centro de Física de Materiales (CSIC-UPV/EHU), Donostia/San Sebastián 20018, Spain; Donostia International Physics Center (DIPC), Donostia/San Sebastián 20018, Spain; ⊙ orcid.org/0000-0002-5265-1441

Ratnadwip Singha — Department of Chemistry, Princeton University, Princeton, New Jersey 08544, United States; orcid.org/0000-0002-3155-2137

Joseph W. Stiles — Department of Chemistry, Princeton University, Princeton, New Jersey 08544, United States; orcid.org/0000-0003-3128-036X

Franziska Kamm – Department of Inorganic Chemistry, University of Regensburg, Regensburg 93040, Germany Florian Pielnhofer – Department of Inorganic Chemistry, University of Regensburg, Regensburg 93040, Germany N. P. Ong – Department of Physics, Princeton University, Princeton, New Jersey 08544, United States Ion Errea — Centro de Física de Materiales (CSIC-UPV/ EHU), Donostia/San Sebastián 20018, Spain; Fisika Aplikatua Saila, Gipuzkoako Ingeniaritza Eskola, University of the Basque Country (UPV/EHU), Donostia/San Sebastián 20018, Spain; Donostia International Physics Center (DIPC), Donostia/San Sebastián 20018, Spain; orcid.org/0000-0002-5719-6580

Maia G. Vergniory – Donostia International Physics Center (DIPC), Donostia/San Sebastián 20018, Spain; Max Planck Institute for Chemical Physics of Solids, Dresden 01187, Germany

Complete contact information is available at: https://pubs.acs.org/10.1021/jacs.3c13535

Notes

The authors declare no competing financial interest.

ACKNOWLEDGMENTS

pubs.acs.org/JACS

This research was primarily supported by the Princeton Center for Complex Materials, a National Science Foundation (NSF)-MRSEC program (DMR-2011750), the Gordon and Betty Moore Foundation's EPIQS initiative (grant numbers GBMF9064 and GBMF9466), and the David and Lucille Packard foundation. C.J.P. is supported by the NSF Graduate Research Fellowship Program under grant number DGE-2039656. G.S. is supported by the Arnold and Mabel Beckman foundation through an AOB postdoctoral fellowship. NSF's ChemMatCARS, Sector 15 at the Advanced Photon Source, Argonne National Laboratory, is supported by the Divisions of Chemistry (CHE) and Materials Research (DMR), National Science Foundation, under grant number NSF/CHE-1834750. This research used resources of the Advanced Photon Source, a U.S. Department of Energy Office of Science user facility operated for the DOE Office of Science by Argonne National Laboratory under Contract no. DE-AC02-06CH11357.M.G.V., I.E., and M.G.A acknowledge the Spanish Ministerio de Ciencia e Innovacion (grants PID2019-109905GB-C21, PID2022-142008NB-I00, and PID2022-142861NA-I00). I.E. acknowledges the Department of Education, Universities and Research of the Eusko Jaurlaritza and the University of the Basque Country UPV/EHU (Grant no. IT1527-22). M.G.V. thanks support to the Deutsche Forschungsgemeinschaft (DFG, German Research Foundation) GA 3314/1-1—FOR 5249 (QUAST) and partial support from European Research Council grant agreement no. 101020833. M.G.A. thanks the Department of Education of the Basque Government for a predoctoral fellowship (grant no. PRE_2019_1_0304). This work has been financially supported by the Ministry for Digital Transformation and of Civil Service of the Spanish Government through the QUANTUM ENIA project call - Quantum Spain project, and by the European Union through the Recovery, Transformation and Resilience Plan - NextGenerationEU within the framework of the Digital Spain 2026 Agenda. C.J.P. acknowledges Scott Lee and Jason Khoury for useful discussions.

REFERENCES

- (1) Haldane, F. D. M. Continuum dynamics of the 1-D Heisenberg antiferromagnet: Identification with the O (3) nonlinear sigma model. *Phys. Lett.* **1983**, 93, 464–468.
- (2) Kitaev, A. Y. Unpaired Majorana fermions in quantum wires. *Phys. Usp.* **2001**, *44*, 131–136.

- (3) Haldane, F. "Luttinger liquid theory" of one-dimensional quantum fluids. I. Properties of the Luttinger model and their extension to the general 1D interacting spinless Fermi gas. *J. Phys. C: Solid State Phys.* **1981**, *14*, 2585–2609.
- (4) Heeger, A. J.; Kivelson, S.; Schrieffer, J. R.; Su, W.-P. Solitons in conducting polymers. *Rev. Mod. Phys.* **1988**, *60*, 781–850.
- (5) Bockrath, M.; Cobden, D. H.; Lu, J.; Rinzler, A. G.; Smalley, R. E.; Balents, L.; McEuen, P. L. Luttinger-liquid behaviour in carbon nanotubes. *Nature* **1999**, *397*, 598–601.
- (6) Wang, P.; Yu, G.; Kwan, Y. H.; Jia, Y.; Lei, S.; Klemenz, S.; Cevallos, F. A.; Singha, R.; Devakul, T.; Watanabe, K.; et al. One-dimensional Luttinger liquids in a two-dimensional moiré lattice. *Nature* **2022**, 605, 57–62.
- (7) Nadj-Perge, S.; Drozdov, I. K.; Li, J.; Chen, H.; Jeon, S.; Seo, J.; MacDonald, A. H.; Bernevig, B. A.; Yazdani, A. Observation of Majorana fermions in ferromagnetic atomic chains on a superconductor. *Science* **2014**, *346*, 602–607.
- (8) Khoury, J. F.; Han, B.; Jovanovic, M.; Singha, R.; Song, X.; Queiroz, R.; Ong, N.-P.; Schoop, L. M. A Class of Magnetic Topological Material Candidates with Hypervalent Bi Chains. *J. Am. Chem. Soc.* **2022**, *144*, 9785–9796.
- (9) Whangbo, M.-H.; Hoffmann, R. The band structure of the tetracyanoplatinate chain. J. Am. Chem. Soc. 1978, 100, 6093-6098.
- (10) Monceau, P. Electronic crystals: an experimental overview. *Adv. Phys.* **2012**, *61*, 325–581.
- (11) Devarakonda, A.; Inoue, H.; Fang, S.; Ozsoy-Keskinbora, C.; Suzuki, T.; Kriener, M.; Fu, L.; Kaxiras, E.; Bell, D. C.; Checkelsky, J. G. Clean 2D superconductivity in a bulk van der Waals superlattice. *Science* **2020**, *370*, 231–236.
- (12) Trump, B. A.; McQueen, T. M. Structure, properties, and disorder in the new distorted-Hollandite PbIr4Se8. *J. Solid State Chem.* **2016**, 242, 112–119.
- (13) Lei, L.; Min, G.; Jun, Y.; Jixiang, G.; Li, P. Synthesis, Structure, and Physical Properties of Single Crystal Hollandite BiIr4Se8. *Chin. J. Low Temp. Phys.* **2018**, *40*, 40–45.
- (14) Wang, X.; Wang, D.; Yin, W.-J.; Si, Y.; Bu, K.; Wang, S.; Zhao, W.; Huang, F. Modulation of the Electronic Structure of IrSe ₂ by Filling the Bi Atom as a Bifunctional Electrocatalyst for pH Universal Water Splitting. *Adv. Energy Sustainability Res.* **2021**, *2*, 2000074.
- (15) Su, W. P.; Schrieffer, J. R.; Heeger, A. J. Solitons in Polyacetylene. *Phys. Rev. Lett.* **1979**, 42, 1698–1701.
- (16) Chiang, C. K.; Fincher, C. R.; Park, Y. W.; Heeger, A. J.; Shirakawa, H.; Louis, E. J.; Gau, S. C.; MacDiarmid, A. G. Electrical Conductivity in Doped Polyacetylene. *Phys. Rev. Lett.* **1977**, 39, 1098–1101.
- (17) Abriel, W.; Rau, F.; Range, K.-J. New compounds A2- xV8O16 (A= K, Tl) with hollandite type structure. *Mater. Res. Bull.* 1979, 14, 1463–1468.
- (18) Batra, N.; Sheet, G. Physics with Coffee and Doughnuts: Understanding the Physics Behind Topological Insulators Through Su-Schrieffer-Heeger Model. *Resonance* **2020**, *25*, 765–786.
- (19) Johannes, M. D.; Mazin, I. I. Fermi surface nesting and the origin of charge density waves in metals. *Phys. Rev. B: Condens. Matter Mater. Phys.* **2008**, 77, 165135.
- (20) Heerwig, A.; Ruck, M. The Low-Valent Bismuth Sulfide Bromide Cu3Bi2S3Br2. Z. Anorg. Allg. Chem. 2011, 637, 1814–1817.
- (21) Wahl, B.; Ruck, M. Ag ₃ Bi ₁₄ Br ₂₁: ein Subbromid mit Bi ₂⁴⁺ -Hanteln und Bi ₉⁵⁺ -Polyedern Synthese, Kristallstruktur und Chemische Bindung. *Z. Anorg. Allg. Chem.* **2008**, *634*, 2873–2879.
- (22) Kalpen, H.; Hönle, W.; Somer, M.; Schwarz, U.; Peters, K.; von Schnering, H. G.; Blachnik, R. Bismut(II)-chalkogenometallate(III) Bi2M4 × 8, Verbindungen mit Bi24+-Hanteln (M = Al, Ga; X = S, Se). Z. Anorg. Allg. Chem. 1998, 624, 1137–1147.
- (23) Perdew, J. P.; Burke, K.; Ernzerhof, M. Generalized Gradient Approximation Made Simple. *Phys. Rev. Lett.* **1996**, 77, 3865–3868.
- (24) Tran, F.; Blaha, P. Accurate Band Gaps of Semiconductors and Insulators with a Semilocal Exchange-Correlation Potential. *Phys. Rev. Lett.* **2009**, *102*, 226401.

- (25) Hoffmann, R. Solids and Surfaces: A Chemist's View of Bonding in Extended Structures; VCH Publishers, 1988; pp 92–98.
- (26) van Smaalen, S.; de Boer, J. L.; Meetsma, A.; Graafsma, H.; Sheu, H.-S.; Darovskikh, A.; Coppens, P.; Levy, F. Determination of the structural distortions corresponding to the q 1-and q 2-type modulations in niobium triselenide NbSe 3. *Phys. Rev. B: Condens. Matter Mater. Phys.* **1992**, 45, 3103–3106.
- (27) Smaalen, S. v.; Lam, E. J.; Lüdecke, J. Structure of the charge-density wave in (TaSe4) 2I. J. Phys.: Condens. Matter 2001, 13, 9923–9936.
- (28) van Smaalen, S.; Bronsema, K.; Mahy, J. The determination of the incommensurately modulated structure of niobium tetratelluride. *Acta Crystallogr. Sect. B Struct. Sci.* **1986**, 42, 43–50.
- (29) Bronsema, K. D.; van Smaalen, S.; De Boer, J.; Wiegers, G. A.; Jellinek, F.; Mahy, J. The determination of the commensurately modulated structure of tantalum tetratelluride. *Acta Crystallogr. Sect. B Struct. Sci.* 1987, 43, 305–313.
- (30) Schutte, W.; De Boer, J. The incommensurately modulated structures of the blue bronzes K0. 3MoO3 and Rb0. 3MoO3. *Acta Crystallogr. Sect. B Struct. Sci.* **1993**, *49*, 579–591.
- (31) Coppens, P.; Petricek, V.; Levendis, D.; Larsen, F. K.; Paturle, A.; Yan, G.; LeGrand, A. D. Synchrotron-radiation study of the five-dimensional modulated phase of tetrathiafulvalene-tetracyanoquinodimethane (TTF-TCNQ) at 15 K. *Phys. Rev. Lett.* **1987**, *59*, 1695–1697.
- (32) Guo, Z.; Sun, F.; Puggioni, D.; Luo, Y.; Li, X.; Zhou, X.; Chung, D. Y.; Cheng, E.; Li, S.; Rondinelli, J. M.; et al. Local Distortions and Metal—Semiconductor—Metal Transition in Quasi-One-Dimensional Nanowire Compounds AV3Q3O δ (A= K, Rb, Cs and Q= Se, Te). *Chem. Mater.* **2021**, 33, 2611–2623.
- (33) Walter, J.; Zhang, X.; Voigt, B.; Hool, R.; Manno, M.; Mork, F.; Aydil, E. S.; Leighton, C. Surface conduction in n-type pyrite FeS 2 single crystals. *Phys. Rev. Mater.* **2017**, *1*, 065403.
- (34) Voigt, B.; Moore, W.; Manno, M.; Walter, J.; Jeremiason, J. D.; Aydil, E. S.; Leighton, C. Transport Evidence for Sulfur Vacancies as the Origin of Unintentional n-Type Doping in Pyrite FeS2. ACS Appl. Mater. Interfaces 2019, 11, 15552–15563.
- (35) Skinner, B.; Chen, T.; Shklovskii, B. I. Effects of bulk charged impurities on the bulk and surface transport in three-dimensional topological insulators. *J. Exp. Theor. Phys.* **2013**, *117*, 579–592.
- (36) Jérome, D. Organic Conductors: From Charge Density Wave TTF-TCNQ to Superconducting (TMTSF) ₂ PF ₆. Chem. Rev. **2004**, 104, 5565–5592.
- (37) Gruner, G. Density Waves in Solids; CRC Press, 1994; pp 55-70
- (38) van Smaalen, S. The Peierls transition in low-dimensional electronic crystals. *Acta Crystallogr., Sect. A* **2005**, *61*, 51–61.
- (39) Fleming, R.; Moncton, D.; McWhan, D. X-ray scattering and electric field studies of the sliding mode conductor Nb Se 3. *Phys. Rev. B: Condens. Matter Mater. Phys.* **1978**, *18*, 5560–5563.
- (40) Fujishita, H.; Sato, M.; Hoshino, S. Incommensurate superlattice reflections in quasi one dimensional conductors,(MSe4) 2I (M= Ta and Nb). *Solid State Commun* 1984, 49, 313–316.
- (41) Sato, M.; Fujishita, H.; Hosnino, S. Neutron scattering study on the structural transition of quasi-one-dimensional conductor K0. 3MoO3. *J. Phys. C: Solid State Phys.* **1983**, *16*, L877–L882.
- (42) Kagoshima, S.; Ishiguro, T.; Anzai, H. X-ray scattering study of phonon anomalies and superstructures in TTF-TCNQ. *J. Phys. Soc. Jpn.* **1976**, *41*, 2061–2071.
- (43) Hoesch, M.; Bosak, A.; Chernyshov, D.; Berger, H.; Krisch, M. Giant Kohn anomaly and the phase transition in charge density wave ZrTe 3. *Phys. Rev. Lett.* **2009**, *102*, 086402.
- (44) Fujishita, H.; Sato, M.; Hoshino, S. X-ray diffraction study of the quasi-one-dimensional conductors (MSe4) 2I (M= Ta and Nb). *J. Phys. C: Solid State Phys.* **1985**, *18*, 1105–1114.
- (45) Lynn, J.; Iizumi, M.; Shirane, G.; Werner, S.; Saillant, R. Neutron-scattering study of the" one-dimensional" conductor K 2 Pt (CN) 4 Br 0.3. 3.2 D 2 O (KCP). *Phys. Rev. B: Condens. Matter Mater. Phys.* 1975, 12, 1154–1166.

- (46) Inami, T.; Ohwada, K.; Kimura, H.; Watanabe, M.; Noda, Y.; Nakamura, H.; Yamasaki, T.; Shiga, M.; Ikeda, N.; Murakami, Y. Symmetry breaking in the metal-insulator transition of BaVS 3. *Phys. Rev. B: Condens. Matter Mater. Phys.* **2002**, *66*, 073108.
- (47) Fleming, R.; Haar, L. W. t.; DiSalvo, F. X-ray scattering study of charge-density waves in K 3 Cu 8 S 6. Phys. Rev. B: Condens. Matter Mater. Phys. 1987, 35, 5388–5391.
- (48) Becker, B.; Patil, N.; Ramakrishnan, S.; Menovsky, A.; Nieuwenhuys, G.; Mydosh, J.; Kohgi, M.; Iwasa, K. Strongly coupled charge-density wave transition in single-crystal Lu 5 Ir 4 Si 10. *Phys. Rev. B: Condens. Matter Mater. Phys.* 1999, 59, 7266–7269.
- (49) Skorupskii, G.; Le, K. N.; Cordova, D. L. M.; Yang, L.; Chen, T.; Hendon, C. H.; Arguilla, M. Q.; Dincă, M. Porous lanthanide metal—organic frameworks with metallic conductivity. *Proc. Natl. Acad. Sci. U.S.A.* **2022**, *119*, No. e2205127119.
- (50) Moya, J. M.; Lei, S.; Clements, E. M.; Kengle, C. S.; Sun, S.; Allen, K.; Li, Q.; Peng, Y. Y.; Husain, A. A.; Mitrano, M.; et al. Incommensurate magnetic orders and topological Hall effect in the square-net centrosymmetric EuGa₂Al₂ system. *Phys. Rev. Mater.* **2022**, *6*, 074201.
- (51) Palatinus, L.; Chapuis, G. SUPERFLIP a computer program for the solution of crystal structures by charge flipping in arbitrary dimensions. *J. Appl. Crystallogr.* **2007**, *40*, 786–790.
- (52) Petříček, V.; Palatinus, L.; Plášil, J.; Dušek, M. Jana2020 a new version of the crystallographic computing system Jana. *Z. für Kristallogr.—Cryst. Mater.* **2023**, 238, 271–282.
- (53) Giannozzi, P.; Baroni, S.; Bonini, N.; Calandra, M.; Car, R.; Cavazzoni, C.; Ceresoli, D.; Chiarotti, G. L.; Cococcioni, M.; Dabo, I.; et al. QUANTUM ESPRESSO: A Modular and Open-Source Software Project for Quantum Simulations of Materials. *J. Phys.: Condens. Matter* 2009, 21, 395502.
- (54) Giannozzi, P.; Andreussi, O.; Brumme, T.; Bunau, O.; Nardelli, M. B.; Calandra, M.; Car, R.; Cavazzoni, C.; Ceresoli, D.; Cococcioni, M.; et al. Advanced Capabilities for Materials Modelling with Quantum ESPRESSO. J. Phys.: Condens. Matter 2017, 29, 465901.
- (55) Dal Corso, A. Pseudopotentials Periodic Table: From H to Pu. Comput. Mater. Sci. 2014, 95, 337–350.
- (56) Methfessel, M.; Paxton, A. T. High-Precision Sampling for Brillouin-zone Integration in Metals. *Phys. Rev. B: Condens. Matter Mater. Phys.* **1989**, 40, 3616–3621.
- (57) Baroni, S.; de Gironcoli, S.; Corso, A. D.; Giannozzi, P. Phonons and Related Crystal Properties from Density-Functional Perturbation Theory. *Rev. Mod. Phys.* **2001**, *73*, 515–562.
- (58) Kresse, G.; Furthmüller, J. Efficiency of Ab-Initio Total Energy Calculations for Metals and Semiconductors Using a Plane-Wave Basis Set. *Comput. Mater. Sci.* **1996**, *6*, 15–50.
- (59) Kresse, G.; Furthmüller, J. Efficient Iterative Schemes for Ab Initio Total-Energy Calculations Using a Plane-Wave Basis Set. *Phys. Rev. B: Condens. Matter Mater. Phys.* **1996**, *54*, 11169–11186.
- (60) Blöchl, P. E. Projector Augmented-Wave Method. *Phys. Rev. B: Condens. Matter Mater. Phys.* **1994**, *50*, 17953–17979.
- (61) Kresse, G.; Joubert, D. From Ultrasoft Pseudopotentials to the Projector Augmented-Wave Method. *Phys. Rev. B: Condens. Matter Mater. Phys.* **1999**, *59*, 1758–1775.
- (62) Dovesi, R.; Erba, A.; Orlando, R.; Zicovich-Wilson, C. M.; Civalleri, B.; Maschio, L.; Rérat, M.; Casassa, S.; Baima, J.; Salustro, S.; Kirtman, B. Quantum-mechanical condensed matter simulations with CRYSTAL. WIREs Comput. Mol. Sci. 2018, 8, No. e1360.
- (63) Dovesi, R.; et al. CRYSTAL17 User's Manual; University of Torino, 2017.
- (64) Perdew, J. P.; Burke, K.; Ernzerhof, M. Generalized Gradient Approximation Made Simple. *Phys. Rev. Lett.* **1996**, 77, 3865–3868.
- (65) Weihrich, R.; Anusca, I. Halbantiperowskite II: zur Kristallstruktur des Pd3Bi2S2. Z. Anorg. Allg. Chem. 2006, 632, 335–342.
- (66) Pielnhofer, F.; Schöneich, M.; Lorenz, T.; Yan, W.; Nilges, T.; Weihrich, R.; Schmidt, P. A rational approach to IrPTe–DFT and CalPhaD studies on phase stability, formation, and structure of IrPTe. Z. Anorg. Allg. Chem. 2015, 641, 1099–1105.

- (67) Heyd, J.; Peralta, J. E.; Scuseria, G. E.; Martin, R. L. Energy band gaps and lattice parameters evaluated with the Heyd-Scuseria-Ernzerhof screened hybrid functional. *J. Chem. Phys.* **2005**, *123*, 174101.
- (68) Ferrero, M.; Rérat, M.; Orlando, R.; Dovesi, R. The calculation of static polarizabilities of 1–3D periodic compounds. the implementation in the crystal code. *J. Comput. Chem.* **2008**, *29*, 1450–1459.
- (69) Ferrero, M.; Rérat, M.; Orlando, R.; Dovesi, R. Coupled perturbed Hartree-Fock for periodic systems: The role of symmetry and related computational aspects. *J. Chem. Phys.* **2008**, *128*, 014110.
- (70) Ferrero, M.; Rérat, M.; Kirtman, B.; Dovesi, R. Calculation of first and second static hyperpolarizabilities of one-to three-dimensional periodic compounds. Implementation in the CRYSTAL code. *J. Chem. Phys.* **2008**, *129*, 244110.